energies

MDPI

Article

Numerical and Experimental Studies on the Effect of Surface Roughness and Ultrasonic Frequency on Bubble Dynamics in Acoustic Cavitation

Rana Altay [1], Abdolali K. Sadaghiani [1,2], M. Ilker Sevgen [1], Alper Şişman [2,3] and Ali Koşar [1,2,4,*]

1 Faculty of Engineering and Natural Sciences, Sabanci University, Tuzla, Istanbul 34956, Turkey; raltay@sabanciuniv.edu (R.A.); a.sadaghiani@sabanciuniv.edu (A.K.S.); ilkersevgen@sabanciuniv.edu (M.I.S.)
2 Sabanci University Nanotechnology and Application Center (SUNUM), Sabanci University, Tuzla, Istanbul 34956, Turkey; alper.sisman@marmara.edu.tr
3 Faculty of Electrical and Electronics Engineering, Marmara University, Kadikoy, Istanbul 34722, Turkey
4 Center of Excellence for Functional Surfaces and Interfaces for Nano-Diagnostics (EFSUN), Sabanci University, Tuzla, Istanbul 34956, Turkey
* Correspondence: kosara@sabanciuniv.edu

Received: 31 January 2020; Accepted: 28 February 2020; Published: 3 March 2020



Abstract: With many emerging applications such as chemical reactions and ultrasound therapy, acoustic cavitation plays a vital role in having improved energy efficiency. For example, acoustic cavitation results in substantial enhancement in the rates of various chemical reactions. In this regard, an applied acoustic field within a medium generates acoustic streaming, where cavitation bubbles appear due to preexisting dissolved gas in the working fluid. Upon cavitation inception, bubbles can undergo subsequent growth and collapse. During the last decade, the studies on the effects of different parameters on acoustic cavitation such as applied ultrasound frequency and power have been conducted. The bubble growth and collapse mechanisms and their distribution within the medium have been classified. Yet, more research is necessary to understand the complex mechanism of multi-bubble behavior under an applied acoustic field. Various parameters affecting acoustic cavitation such as surface roughness of the acoustic generator should be investigated in more detail in this regard. In this study, single bubble lifetime, bubble size and multi-bubble dynamics were investigated by changing the applied ultrasonic field. The effect of surface roughness on bubble dynamics was presented. In the analysis, images from a high-speed camera and fast video recording techniques were used. Numerical simulations were also done to investigate the effect of acoustic field frequency on bubble dynamics. Bubble cluster behavior and required minimum bubble size to be affected by the acoustic field were obtained. Numerical results suggested that bubbles with sizes of 50 μm or more could be aligned according to the radiation potential map, whereas bubbles with sizes smaller than 10 μm were not affected by the acoustic field. Furthermore, it was empirically proven that surface roughness has a significant effect on acoustic cavitation phenomena.

Keywords: acoustic cavitation; surface roughness; cavitation bubble; bubble dynamics; bubble size; bubble growth

1. Introduction

Acoustic cavitation is a liquid to vapor phase change phenomenon and takes place within a medium due to the effect of ultrasonic pressure fluctuations. These ultrasonic pressure fluctuations result in the formation of bubbles from preexisting dissolved gases, which is followed by the subsequent growth and violent collapse of bubbles. The occurrence of bubble collapses generate local high pressures

and a temperature rise up to 10^5 K [1], which lead to severe physical impact, shock wave radiation [2,3], turbulence, microjets and chemical reactions [4] and could be exploited in many applications such as cancer treatment [5–7], ultrasonic cleaning [8–10], wastewater treatment [11–13], nanomaterials synthesis [14,15], biomedical applications [16] and emulsification [17–19].

Although the growth and collapse of bubbles in acoustic cavitation are widely used in many different applications, there are some disadvantages of acoustic cavitation. The consequences of bubble collapse as shock waves, temperature change, or a formation of a liquid jet might lead to cavitation erosion. Due to the erosion, crevices on surfaces might form or stress fatigue might occur. Moreover, the formation of bubbles might cause a decrease in the device efficiency [20]. To understand the effect of acoustic cavitation and its damage on different materials, some studies were recently performed. For example, Abedini et al. [21] investigated corrosion and material alterations of $CuZn_{38}Pb_3$ brass under acoustic cavitation during different sonication durations (maximum duration of 5 h). They reported that the corrosion rate, plastic deformation and surface roughness were larger for longer sonication periods. Also, the damage due to the cavitation varied according to the α-β′ phases of brass alloy.

The aim of understanding the underlying mechanisms makes fundamental studies attractive starting from the 1940s (Blake, [22]). In 1949, Blake reported bubble growth in an applied acoustic field and covered rectified diffusion and bubble-bubble coalescence [22]. Later, Noltingk and Neppiras [23] performed a study, where equations of cavitation bubble growth, pressure and velocity distribution were derived for acoustic cavitation. A year later in 1951, they reported that some parameters limited acoustic cavitation [24], which were listed as pressure amplitude, pressure wave frequency, bubble core radius, and hydrostatic pressure. In 1960, Leith [25] explained the negative effects of cavitation on metals and liquid characteristics due to bubble collapse and cavitation erosion.

With the advances in related technology, the number of studies in this field increased. In 1996, Tian et. al. captured the oscillations due to microbubble generation under an acoustic field, using a Charge-coupled device (CCD) camera [26]. An analysis on the bubble size based on the levitation in water was made. Similarly, Mettin [27] implemented high-speed imaging techniques for visualization of different bubble shapes/structures such as conical shape, cluster and double layer, which formed at low applied frequencies. Recently, Reuter et al. [28] studied bubble size and its distribution in various acoustic structures. A high-speed camera was used for the analysis of bubbles during the oscillation at a low applied frequency. There are other different techniques for bubble dynamics analysis at an applied ultrasonic frequency such as light scattering [29] and stroboscopy [30].

Many recent efforts have focused on changing the bubble distribution by applying different powers and frequencies. The dynamic responses of bubbles according to the change of these parameters were included in the literature [8,31–36]. For example, Brotchie et al. [31] obtained bubble distribution at different applied frequencies and powers in their experimental study. They observed that bubble size and ultrasound frequency had an inverse relationship, and the bubble size was proportional to the acoustic power. In the study of Sunartio et. al. [37], the effects of varying frequency and power on acoustic bubble coalescence were revealed in the presence of surface-active solutes by calculating the volume change of the dispersion after each sonication period. They reported surface assimilation in the bubbles due to the usage of surface-active solutes, which caused a delay in bubble coalescence. Furthermore, the alteration of power did not have any effect on the dynamics of bubble coalescence. Yet, frequency variation caused a change in bubble coalescence, where short range steric revulsion was dominant. Ashokkumar also reported the effect of surface-active solutes present in the experimental medium, and bubble growth and coalescence were in-depth discussed in this study [38]. To provide a different perspective, Zhou [39] used acoustic cavitation in pool boiling experiments to analyze its effect on boiling heat transfer enhancement. It was reported that the use of acoustic cavitation in pool boiling experiments decreased the superheat, and emerging bubbles increased heat and mass transfer, which led to enhanced boiling heat transfer. The study by Fang et al. [13] focused on wastewater treatment with acoustic cavitation. Acoustic cavitation in this study served for propagation of the

plasma in water by the formation of micro bubbles. Cui et al. [40] used acoustic cavitation to treat crude oil. Accordingly, shorter branched chain and relatively short alkanes compared to the initial version could be achieved. Meanwhile, asphaltene molecules were polymerized.

While many studies displayed the effect of major parameters on acoustic cavitation and bubble dynamics, the surface roughness effect on acoustic cavitation bubbles has not been studied in the literature to the best knowledge of the authors. In this study, bubble dynamics was investigated for different surface roughness and applied frequency values. For visualization, a high-speed camera was used for recording videos/images. Thus, growth and collapse of cavitation bubbles could be captured for different surface roughness and frequency values. To validate the obtained results, numerical simulations of acoustic streaming and particle trajectory analysis of air bubbles in a medium were also performed.

2. Materials and Methods

2.1. Experimental Setup

The schematic of the experimental setup is shown in Figure 1. A cubic pool made of the glass with dimensions of $15 \times 15 \times 15$ cm^3 was used for visualization of the cavitation experiments. The working fluid was chosen as water. A Langevin type piezoelectric transducer, which generates mechanical movements from electrical signals, was operated at frequencies of 28 kHz and 40 kHz. Mountable disc surfaces with a diameter of 40 mm and different surface roughness values (of 100 nm and 1 µm) were utilized to investigate the effect of surface roughness at the applied frequency of 40 kHz (shown in Figure 1b). Roughness on the surface was achieved with a sandpaper. The transducer was fixed at the top of the pool. A high-speed camera, which allows for fast recording of the videos and snapshots of the bubbles during acoustic cavitation phenomena with exposure time of 2 µs, frame rate of 10,000, was used for visualization. The visualization was achieved using the Shadowgraph Imaging Technique.

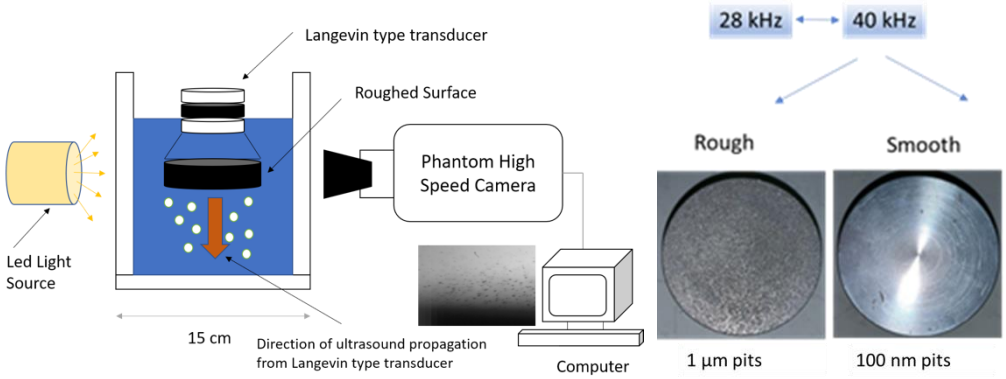


Figure 1. Description of experimental setup and mountable surfaces: (**a**) Schematic representation of the experimental setup; (**b**) Mountable surfaces with different surface roughness values.

The shadowgraph images of acoustic cavitation were captured by a high-speed camera. In this study, parallel-light direct shadowgraph was used. Accordingly, when the light beam passes through the bubble, the light is focused. The strongest light refraction is at the boundary between the bubble and surrounding water. No refraction occurs outside the bubble or exactly at its center. A dark circular shadow marks the periphery of the bubble. Inside it, there is a brighter illuminance ring, which is the light displaced from the dark circular shadow.

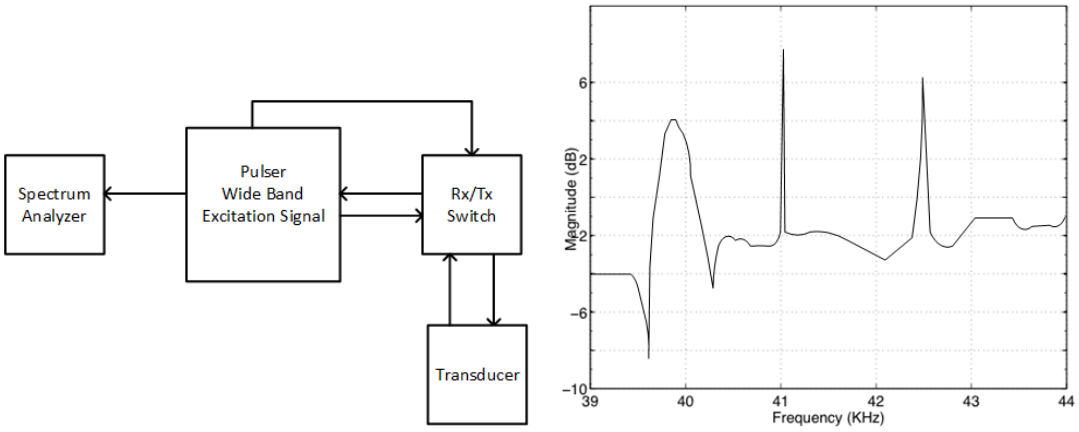
The camera was connected to the workstation to analyze bubble dynamics. The direction of the ultrasound application (from the transducer) was from top to the bottom of the pool. To ensure the repeatability and reliability of the experiments, every experiment was performed for three times.

The high-speed camera was located on the side of the pool such that the surface of the transducer and 500 µm above of the surface could be recorded for acoustic cavitation.

2.2. Acoustic Characterization and Control Circuit

Cavitation bubbles were generated using a sandwich-type ultrasonic transducer. The electronics to drive this type of transducer mostly uses a digitally controlled push-pull transistor stage. To prevent any short circuit, the transistor excitation timing is crucial for this type of design [41–45]. In this study, a new driver circuit, which uses a simple function generator, was designed. The new design simplifies electronics and reduces system complexity.

The sandwich-type transducers are used inside many industrial devices and are well characterized [46,47]. The transducer usually has a single operating band, which has a fractional bandwidth of around 5%. The operation frequency band was investigated using the experimental setup depicted in Figure 2a. A pulse generator (5072PR, Olympus CO. Waltham, MA, 02453, USA) excited the transducer using a wideband pulse, and the received echo was measured by a spectrum analyzer (DSA875, Rigol, Beaverton, OR 97008, USA). The measure response showed a narrow band characteristic with an operating frequency of 39.85 kHz (Figure 2b). The setup was used to determine the exact operating frequency so that the transducer could be driven effectively.



(a) (b)

Figure 2. Characterization and measurement of transducer: (**a**) Transducer characterization setup; (**b**) The measured frequency characteristics of a 40 kHz transducer.

The narrowband behavior of the transducer increased the dependency of efficiency on the excitation frequency (e.g., 0.3% of the change in frequency would result in 20% of the change in the power transmitted to the system). Hence the frequency stability had a significant effect on providing constant power.

The designed driver circuitry was able to set the desired frequency and power level. The circuit was controlled by a digital signal in order to provide frequency stability. Unlike the usual design, a single switch was employed in the design. The high voltage switch pumped the electrical power to the transducer by a predefined frequency. The switch was a metal-oxide semiconductor (MOS) transistor connected to a high voltage direct current (HV-DC) supply, which was provided from rectified alternating current (AC) voltage (220 V RMS). In the design, only a single switch was used. It charged the piezoelectric transducer during on-time, and the accumulated charge was discharged in off-time. The main component was inversely positioned fast diodes in the discharging circuitry. Hence, only one switch was used to simplify the excitation circuit of the MOS transistor. A simple function generator applied the pulse width modulated (PWM) signal to operate the system. The duty cycle of the PWM signal defined the power (duty cycle must be under 40%), and the PWM frequency determined the transducer's operation point. The block schematic explaining the circuit design is

given in Figure 3a. The voltage across transducer nodes can be seen in Figure 3b, and the frequency domain representation of the voltage shows that the transducer is actuated by a pretty narrow band signal around the required frequency (Figure 3c).

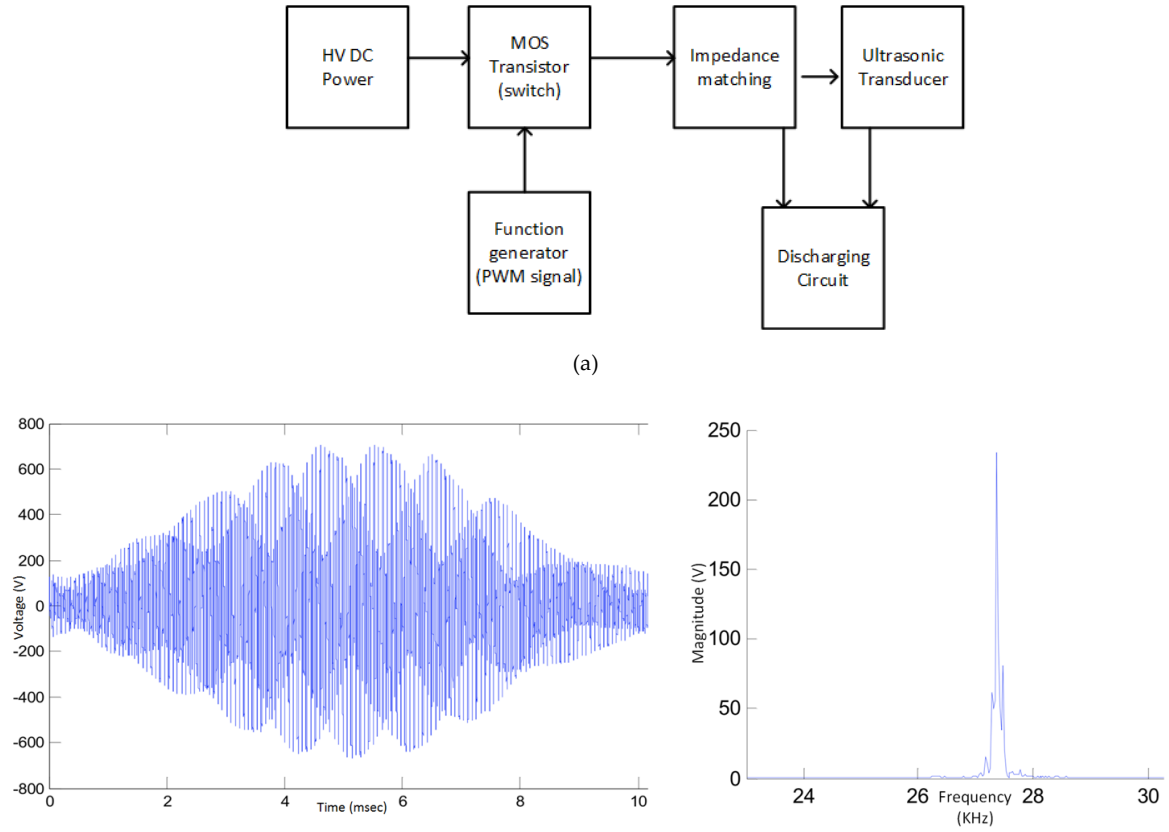


Figure 3. Schematic and characterization of utilized electronic circuit: (**a**) The block schematic of the designed circuit; (**b**) Measured voltage when transducer is actuated by 26.7 kHz; (**c**) The frequency domain representation of the voltage waveform given in (**b**).

2.3. Numerical Analysis

The COMSOL 5.4 software was used for solving the governing equations. Acoustic and particle tracking modules were used to investigate the effect of acoustic field on air bubbles. Air bubbles were considered as spherical particles with diameters ranging from 10 µm to 50 µm. Acoustophoretic radiation, gravity and drag forces were implemented in the numerical domain. Open boundary conditions were considered for side walls, while plane wave radiation was defined as the transducer surface. The conservation equations for an acoustic wave propagation into a fluid are given as:

$$\nabla\left(\frac{1}{\rho}\nabla P\right) - \frac{1}{\rho c^2}\cdot\frac{\partial^2 P}{\partial t^2} = 0 \tag{1}$$

Here, P, ϱ, c, and t are pressure, density, sound velocity in medium (water), and time, respectively. For a $P(r,t) = P(r)\cdot e^{i\omega t}$ solution, where $r = r(x,y,z)$ is the position vector, $\omega = 2\pi f$ is angular frequency, and f is the frequency. Substituting the pressure distribution into Equation (1), the acoustic pressure $P(r)$ is obtained as:

$$\nabla\left(\frac{1}{\rho}\nabla P\right) - \frac{\omega^2}{\rho c^2}P = 0 \tag{2}$$

The intensity distribution is expressed as:

$$I(r) = \frac{p(r)^2}{2\rho c} \tag{3}$$

After mesh dependency analysis, the homogeneous pressure equation was solved as:

$$P(r,t) = Ae^{i(\omega t - kr)} \tag{4}$$

3. Results and Discussion

3.1. Single Bubble Dynamics in an Acoustic Field

When appropriate ultrasonic radiation is applied, "multi-bubbles" appear in a liquid medium. The generated bubbles can be formed due to either the existence of the dissolved gas nuclei or the caged gases in the solid particles. Another reason for the formation of bubbles can be attributed to the separation of larger bubbles in the liquid medium. Theoretically, if the bubble overcomes the pressure threshold, which is called the Blake threshold, P_B, (Equation (5)), nucleation takes place [1]:

$$P_B = P_0 + \frac{8\sigma}{9}\sqrt{\left(\frac{3\sigma}{2\left[P_0 + (2\sigma/R_B)R_B^3\right]}\right)} \tag{5}$$

where P_0, R_B and σ are the ambient pressure, Blake radius and surface tension, respectively. Upon nucleation, the bubble can start to grow and go through stable cavitation for a large driving acoustic pressure. On the other hand, if the driving acoustic pressure is low, the bubbles dissolve in the medium. For much higher acoustic pressures, which exceed the cavitation threshold, the bubbles become unstable or transient. In another scenario, larger bubbles can be affected by the buoyancy force and move up to the surface of the liquid medium, which is referred as "degassing".

The bubble growth process at an applied ultrasonic frequency is mainly separated into two different mechanisms: rectified diffusion and coalescence. The coalescence occurs due to the secondary Bjerknes force [48] between two oscillating bubbles in the same oscillation phase. They merge and form a bigger bubble. The growth of the bubbles via the coalescence mechanism is faster than the rectified diffusion. Figure 4 represents the rectified diffusion, in which the sinusoidal acoustic streaming affects the bubble dynamics and causes periodical growth and wane. During the growth, the expansion takes place, the inner pressure of the bubble is low, and the diffusion of gas into the bubble occurs. Inversely, the diffusion of the gas out of the bubble appears at the time of compression. After the bubble reaches the critical maximum size, the bubble collapse occurs which leads to pressure shockwaves.

An example of a single bubble lifetime at the applied 40 kHz acoustic field frequency is shown in Figure 5a. The experiment is conducted with a smooth transducer surface. By using fast video recording, the rectified diffusion of the single bubble was recorded in every 150 µs, as shown in Figure 5b. The bubble goes through the rectified diffusion, and its size alters according to the inside pressure. The pressure difference between the liquid medium and the inner bubble allows for the periodic growth, expansion and compression of the bubble over several cycles. After 750 µs, the bubble reaches the maximum size, which is found as approximately 35 µm, which is followed by the violent collapse of the bubble.

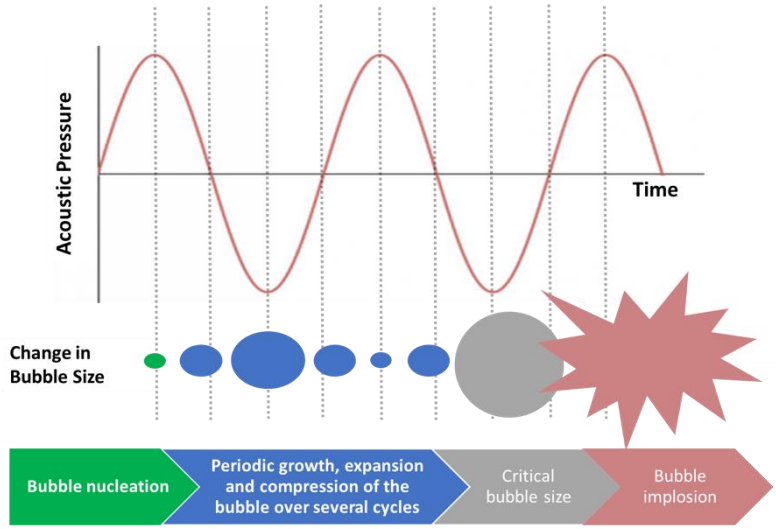
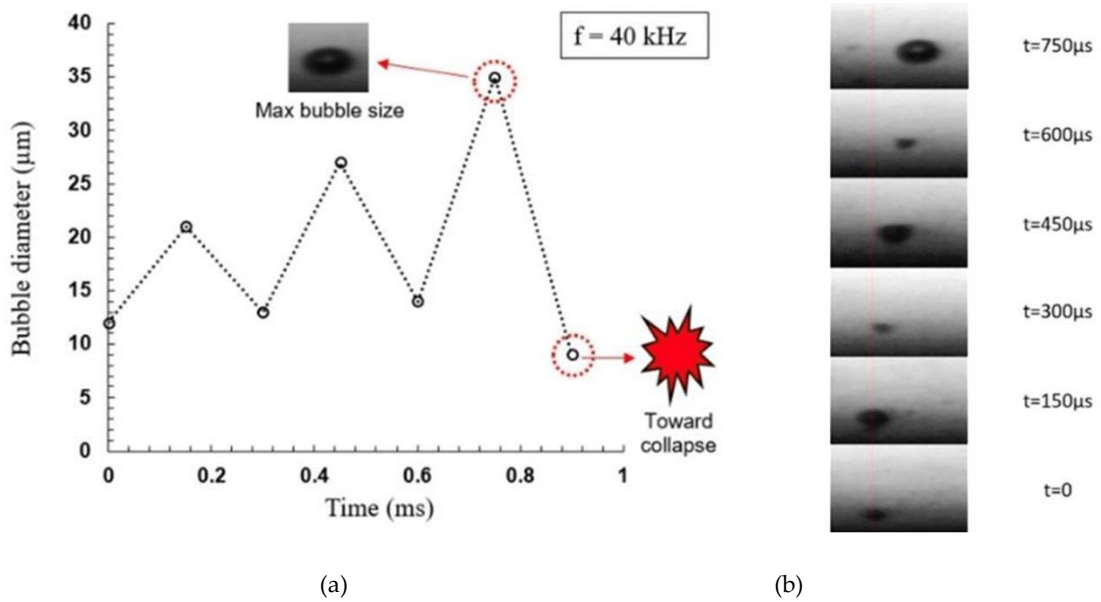


Figure 4. Rectified diffusion mechanism under the effect of sinusoidal acoustic streaming.



(a) (b)

Figure 5. Size variation of a single bubble in an acoustic field: (**a**) Schematic representation of the single bubble lifetime at an applied frequency of 40 kHz; (**b**) Captured images of rectified diffusion of the single bubble.

3.2. Bubble Behavior in Acoustic Field

Acoustic streaming is of sinusoidal nature, which causes pressure fluctuations in the liquid medium. As a result of an applied acoustic field, the formation of multi-bubble clouds occurs. To analyze the multi-bubble behavior under acoustic field, the high-speed camera was used for visualization. The shooting range was set to 100 μs. The frequency of applied ultrasound was chosen as 40 kHz, and the transducer surface with surface roughness value of 100 nm was used. Figure 6 shows a snapshot of multi-bubble clouds within 100 μs time intervals. It can be observed that the compression and rarefaction of the bubble clouds can be seen according to the pressure nodes in the applied ultrasound wave.

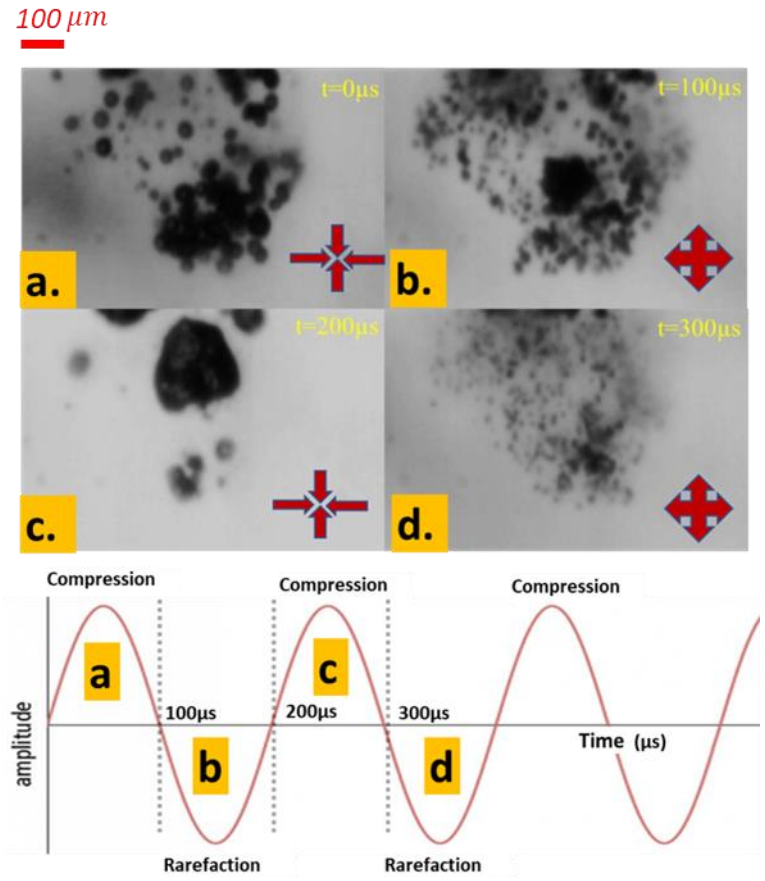
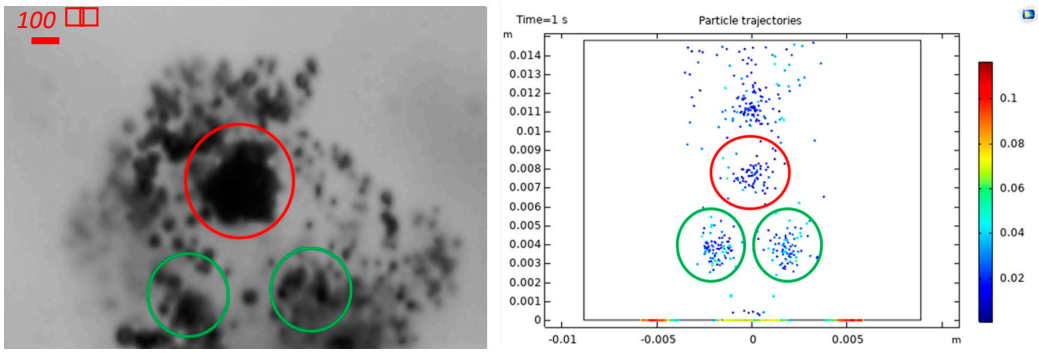


Figure 6. The multi-bubble cloud's behavior during 300 μs at the applied acoustic field of 40 kHz: (**a**) and (**c**) compression cycle, (**b**) and (**d**) rarefaction cycle.

During the compression cycle, the cloud shrinks, which is followed by their expansion, where the amplitude of the acoustic pressure switches into the lower node. As a result, similar behavior to the single bubble case can be observed for multi-bubbles at the same applied acoustic frequency.

To provide further understanding about the effect of acoustic field on bubble dynamics, numerical modeling was performed using the COMSOL® software (Burlington, MA 01803 USA) [49]. According to the experimental results shown in Figure 7a, locally grouped bubble clouds in the liquid are visible. This behavior can be also recognized in simulated air particle trajectories shown in Figure 7b. According to the comparison between experimental and numerical results, almost the same bubble distribution can be achieved.



(a) (b)

Figure 7. Bubble cloud formation (**a**) experimental results (**b**) numerical results for the response of air particles to the applied acoustic field.

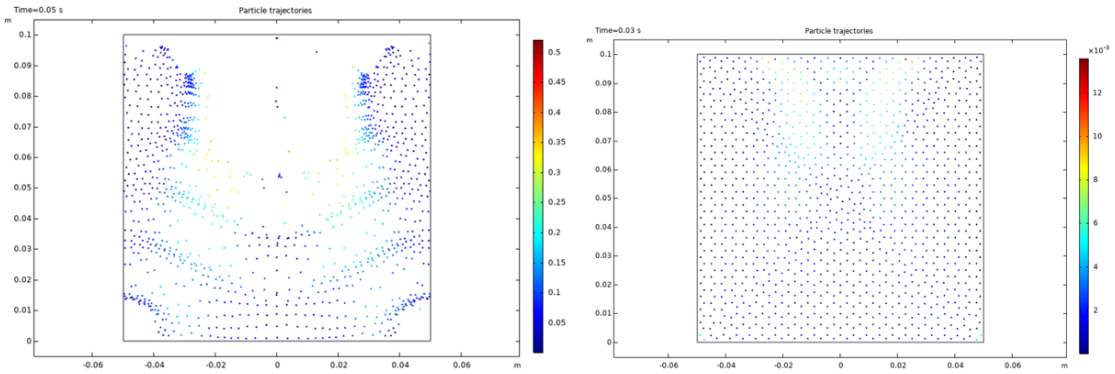
An oscillating flow field can be described as an acoustic wave with infinite wavelength. The flow velocity is expressed as $u_c(t) = \hat{u}_c \sin(\omega_f t)$, where $\hat{u}_c$ is the amplitude of the velocity wave and $\omega_f = 2\pi f_r$ is the angular frequency. Resonance size, Stokes number, $S_t = f_r/c$, and density ratio, $\gamma = \rho_p/\rho_l$, are major parameters affecting the response of air particles to the acoustic field.

The acting radiation force on the bubbles inside the medium is due pressure gradient expressed as $\frac{\partial P}{\partial x} = -\rho\frac{Du}{Dt}$. In addition to the primary radiation force, which acts in the direction of acoustic wave propagation, a secondary radiation force manipulates the agents to attract or repel each other. The time-dependent radiation force on the bubble can be calculated from the driving pressure wave and time-dependent volume of the bubble. Furthermore, the translational motion of the bubble in response to the radiation force can be calculated by solving the equations of air particle trajectory. For an air particle with mass of $m_b = \rho V_b$, the particle trajectory equation is given as $m_b\frac{du_b}{dt} = F_R(t) + F_{QS}(t)$. The radiation force ($F_R(t)$) and quasi-static drag force ($F_{QS}(t)$) are expressed as:

$$F_R(t) = -V_b\frac{dP_{driv}}{dx} \tag{6}$$

$$F_{QS}(t) = \frac{1}{2}\rho_l|u_r|u_r A\frac{24}{\frac{2R|u_l-u_b|}{\upsilon}}\left(1+0.197\left(\frac{2R|u_l-u_b|^{0.63}}{\upsilon}\right)\right) \tag{7}$$

Here, m_b is the air particle mass, u_b is the air particle velocity, dP_{driv} is the driving pressure difference, u is the velocity, $u_r = u_l - u_b$ is the relative velocity, and υ is the viscosity. To examine the effect of radiation force, the motion of bubbles with different diameters was simulated at the 40 kHz ultrasonic frequency. The obtained results are shown in Figure 8. Accordingly, the bubbles with diameters smaller than 10 µm are not affected by the acoustic field, while bubbles with diameters larger than 50 µm can be sorted according to the radiation potential map. The obtained results indicate that the response of air particles to the radiation force is proportional to their size, which is also displayed by the visual images shown in Figure 7a.



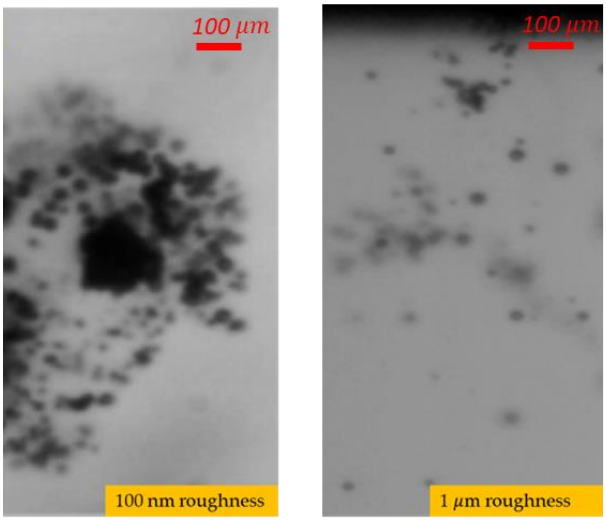
(a) (b)

Figure 8. Simulation results of bubble trajectories with the bubbles having different sizes at the applied frequency of 40 kHz (**a**) Air bubble having 50 µm diameter; (**b**) Air bubble having 10 µm diameter.

3.3. Effect of Surface Roughness and Ultrasonic Frequency

Figure 9 shows the acoustic cavitation induced bubbles at the applied ultrasonic frequency of 40 kHz when different surfaces are mounted on the transducer. The images were taken with the high-speed camera and 100 µs time slots. Figure 9a displays the multi-bubble formation when the smooth surface (with 100 nm surface roughness) is tested. The bubbles appear and form a cloud. Meantime, the bubbles on the rough surface exhibit more disorganized behavior. As a result, the cavity length diminution is evident with the increase in the roughness.

When a single acoustic cavitation bubble collapses in the liquid medium, the temperature can be locally increased up to 10,000 K [1]. The pool temperatures were measured at four different locations. The average temperature of four thermocouples were recorded for analysis purposes. The experiments were conducted under the 40 kHz applied ultrasonic field.



(a) (b)

Figure 9. The cavitation bubbles at 40 kHz. (**a**) Multi-bubble cloud formation on a smooth surface with 100 nm roughness; (**b**) Disorganized bubbles with diminution of cavity length on a rough surface with 1 μm roughness.

The temperature variations of the pool with time are shown in Figure 10. Accordingly, for surface roughness of 100 nm, the temperature increases from 299 K (room temperature) to 340 K after 35 minutes of experimentation. The reason for the temperature rise can be the energy released during the bubble collapse. On the other hand, for the surface with surface roughness parameter Ra = 1 μm, the pool temperature is stabilized within a shorter time (almost 25 minutes). Here, Here, Ra is the arithmetical mean deviation of the assessed profile and is calculated as $Ra = \frac{1}{n}\sum_{i=1}^{n}\left|y_i\right|$, where, y_i is the vertical distance from the mean line to the ith data point. Moreover, the pool temperature is 10 K colder than the previous case (smooth surface), which is due to lower intensity of cavitation inside the pool for the case of rough surface.

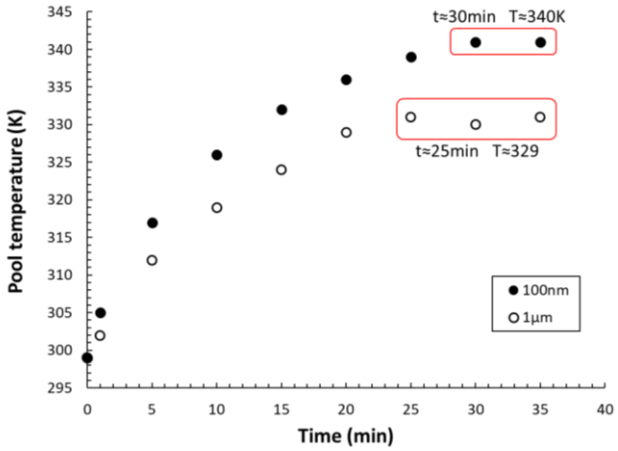


Figure 10. The temperature rise during the acoustic cavitation experiments at the applied frequency of 40 kHz.

To observe the effect of applied ultrasonic frequency on acoustic cavitation, 28 kHz and 40 kHz are applied. For all the experiments, the smooth surface transducer surface is tested. At the 40 kHz applied frequency, more frequent fluctuations cause many but smaller bubbles than the case of 28 kHz.

While more detailed and extensive studies are required for accurate assessment of energy efficiency in energy conversion processes involving cavitation, the reported results clearly prove that the surface roughness has a significant effect on acoustic cavitation phenomena. This is evident from the maximum pool temperature (Figure 10) and bubble size (Figure 11). Although the motivation behind acoustic cavitation strongly depends on the applications (sonoporation, ultrasonic cleaning, and chemical reactor), control of acoustic cavitation using surface roughness could be an effective passive approach for energy efficiency applications.

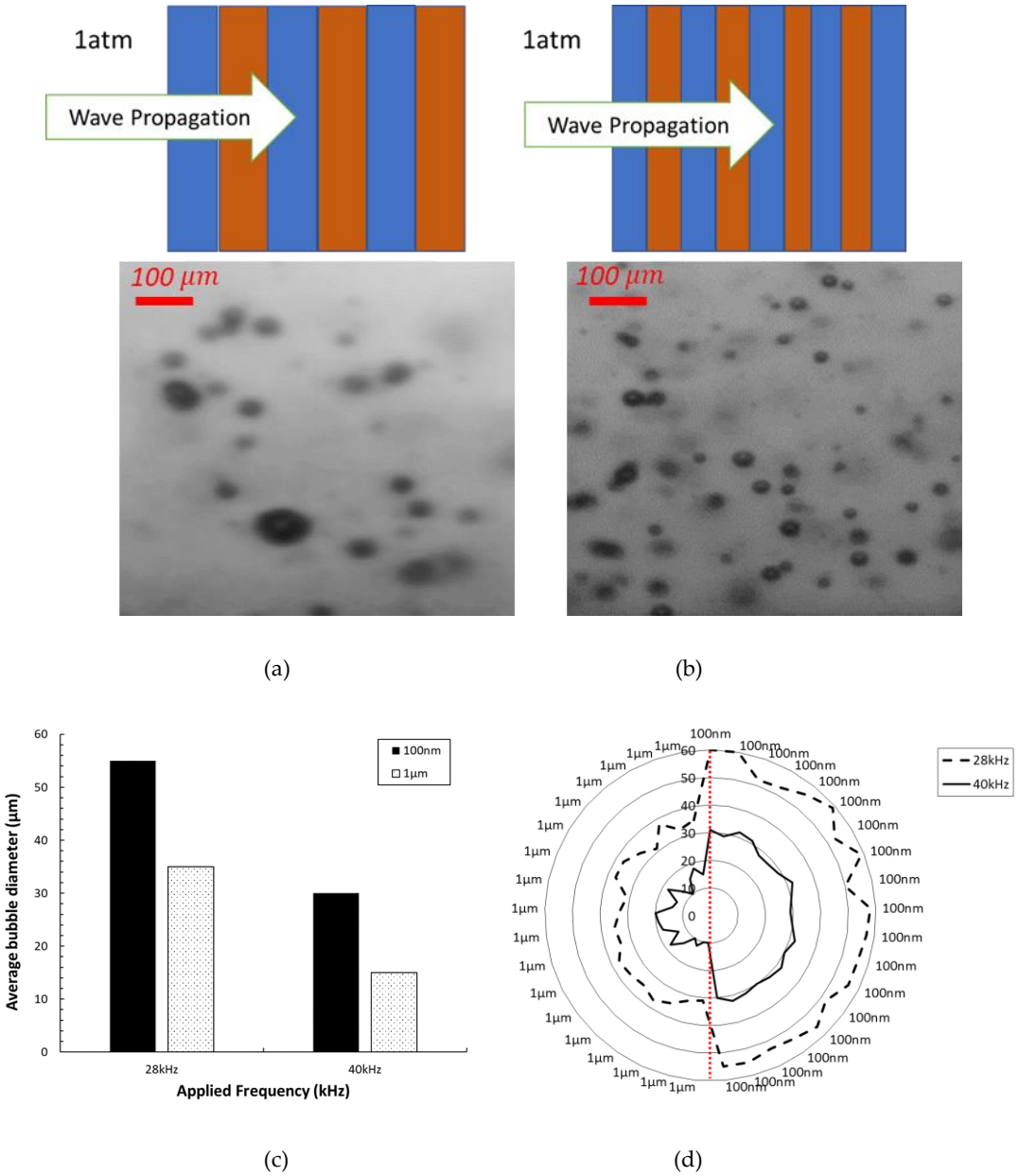


Figure 11. The bubbles with different shape and quantity on the surface with Ra = 1 μm under the effect of different applied frequencies (**a**) Bubbles occurrence at 28 kHz; (**b**) Bubbles occurrence at 40 kHz. (**c**) Average bubble diameters at different acoustic field frequencies and surface roughness parameters (**d**) distribution of the nucleated bubbles at different acoustic field frequency and surface roughness parameter.

As seen in Figure 11a, there are approximately 20 bubbles, whereas 50 bubbles are visible on the same scale in Figure 11b. The average size of generated bubbles under the 40 kHz acoustic field is almost twice as much as the size of generated bubbles under the 28 kHz acoustic field. As the size of bubbles increases, the generated energy due to bubble collapse remarkably decreases. Furthermore, as can be seen in Figure 11c, surface roughness reduces the bubble size. The main reason is the propagation angle of surface acoustic wave propagation. As surface roughness increases, surface wave propagation occurs with lower velocity, and scattering increases, thereby weakening the wave.

4. Conclusions

This study was performed to provide more information about the effect of surface on acoustic cavitation at two widely used applied ultrasonic frequencies below 50 kHz. The investigation of the effect of surface within this range is critical for many applications such as ultrasonic cleaning and drug delivery. The effect of surface roughness on bubble dynamics in acoustic cavitation was experimentally and numerically investigated. Surfaces with roughness values of 100 nm and 1 µm were examined in the 28 kHz and 48 kHz acoustic fields. DI-water was used as the working fluid. A high-speed camera was used to capture bubble dynamics inside the pool. Single bubble lifetime was investigated based on visual results. The average bubble sizes for different conditions were obtained and tabulated. It was found that surface roughness reduced the bubble size. The numerical analysis indicated that the bubbles with diameters smaller than 10 µm were not affected by the acoustic field, while bubbles with a diameter of 50 µm could be sorted according to the radiation potential map. The obtained results showed that the response of air bubbles to the radiation force was proportional to their size. The recorded pool temperatures revealed that the pool temperature was stabilized within a shorter time (almost 10 minutes shorter) for the surface with Ra = 1 µm. Moreover, the pool temperature was 10 K colder than the previous case (smooth surface), which was due to lower intensity of cavitation inside the pool for the case of rough surface. More studies are required in this field to deepen the understanding about the effect of surface on plane wave propagation and subsequent acoustic cavitation within the medium.

Author Contributions: Conceptualization, Methodology, Validation: R.A. and A.K.S.; Software, Setup preparation: M.I.S.; Acoustic Circuit Design: A.Ş.; Supervision: A.K. All authors have read and agreed to the published version of the manuscript.

Funding: This research received no external funding.

Acknowledgments: The equipment and characterization support provided by the Sabanci University Nanotechnology Research and Applications Center (SUNUM) and its staff members are appreciated.

Conflicts of Interest: The authors declare no conflict of interest.

Nomenclature

Parameter	Description
c	Sound velocity (m/s)
f	Frequency (1/s)
F_R	Radiation force (N)
F_{QS}	Quasi-static drag force (N)
k	Wave number (1/m)
P	Pressure (kPa)
P0	Ambient pressure (kPa)
R	Bubble radius (m)
St	Stokes number (-)
t	Time (s)
u(t)	Velocity (m/s)
u_r	Relative velocity (m/s)
V	Velocity (m/s)

Greek letters

ϱ	Density (kg/m^3)
ω	Angular frequency (1/s)
σ	Surface tension (N/m)
γ	Density ration (-)
ν	Kinematic viscosity (m^2/s)

Abbreviations

CCD	Charge-coupled device
MOS transistor	Metal–oxide–semiconductor transistor
HV-DC	High-voltage direct current
AC	Alternating current
PWM signal	Pulse-width modulation signal

References

1. Leong, T.; Ashokkumar, M.; Kentish, S. The growth of bubbles in an acoustic field by rectified diffusion. *Handb. Ultrason. Sonochemistry* **2016**, *10*, 978–981.
2. Holzfuss, J.; Rüggeberg, M.; Billo, A. Shock wave emissions of a sonoluminescing bubble. *Phys. Rev. Lett.* **1998**, *81*, 5434. [CrossRef]
3. Peshkovsky, S.L.; Peshkovsky, A.S. Shock-wave model of acoustic cavitation. *Ultrason. Sonochemistry* **2008**, *15*, 618–628. [CrossRef]
4. Suslick, K.S.; Didenko, Y.; Fang, M.M.; Hyeon, T.; Kolbeck, K.J.; McNamara III, W.B.; Mdleleni, M.M.; Wong, M. Acoustic cavitation and its chemical consequences. *Philos. Trans. R. Soc. Lond. Ser. A Math. Phys. Eng. Sci.* **1999**, *357*, 335–353. [CrossRef]
5. Sazgarnia, A.; Shanei, A.; Taheri, A.R.; Meibodi, N.T.; Eshghi, H.; Attaran, N.; Shanei, M.M. Therapeutic effects of acoustic cavitation in the presence of gold nanoparticles on a colon tumor model. *J. Ultrasound Med.* **2013**, *32*, 475–483. [CrossRef]
6. Coussios, C.; Farny, C.; Ter Haar, G.; Roy, R. Role of acoustic cavitation in the delivery and monitoring of cancer treatment by high-intensity focused ultrasound (HIFU). *Int. J. Hyperth.* **2007**, *23*, 105–120. [CrossRef]
7. Aw, M.S.; Paniwnyk, L.; Losic, D. The progressive role of acoustic cavitation for non-invasive therapies, contrast imaging and blood-tumor permeability enhancement. *Expert Opin. Drug Deliv.* **2016**, *13*, 1383–1396. [CrossRef]
8. Yusof, N.S.M.; Babgi, B.; Alghamdi, Y.; Aksu, M.; Madhavan, J.; Ashokkumar, M. Physical and chemical effects of acoustic cavitation in selected ultrasonic cleaning applications. *Ultrason. Sonochemistry* **2016**, *29*, 568–576. [CrossRef]
9. Muthukumaran, S.; Yang, K.; Seuren, A.; Kentish, S.; Ashokkumar, M.; Stevens, G.W.; Grieser, F. The use of ultrasonic cleaning for ultrafiltration membranes in the dairy industry. *Sep. Purif. Technol.* **2004**, *39*, 99–107. [CrossRef]
10. Bryson, L.; Fernandez Rivas, D.; Boutsioukis, C. Cleaning of used rotary nickel-titanium files in an ultrasonic bath by locally intensified acoustic cavitation. *Int. Endod. J.* **2018**, *51*, 457–468. [CrossRef]
11. Pradhan, A.A.; Gogate, P.R. Degradation of p-nitrophenol using acoustic cavitation and Fenton chemistry. *J. Hazard. Mater.* **2010**, *173*, 517–522. [CrossRef]
12. Pétrier, C.; Francony, A. Ultrasonic waste-water treatment: Incidence of ultrasonic frequency on the rate of phenol and carbon tetrachloride degradation. *Ultrason. Sonochemistry* **1997**, *4*, 295–300. [CrossRef]
13. Fang, Y.; Hariu, D.; Yamamoto, T.; Komarov, S. Acoustic cavitation assisted plasma for wastewater treatment: Degradation of Rhodamine B in aqueous solution. *Ultrason. Sonochemistry* **2019**, *52*, 318–325. [CrossRef]
14. Xu, H.; Zeiger, B.W.; Suslick, K.S. Sonochemical synthesis of nanomaterials. *Chem. Soc. Rev.* **2013**, *42*, 2555–2567. [CrossRef]
15. Han, J.T.; Jang, J.I.; Kim, H.; Hwang, J.Y.; Yoo, H.K.; Woo, J.S.; Choi, S.; Kim, H.Y.; Jeong, H.J.; Jeong, S.Y. Extremely efficient liquid exfoliation and dispersion of layered materials by unusual acoustic cavitation. *Sci. Rep.* **2014**, *4*, 5133. [CrossRef]

16. Hockham, N.; Coussios, C.C.; Arora, M. A real-time controller for sustaining thermally relevant acoustic cavitation during ultrasound therapy. *IEEE Trans. Ultrason. Ferroelectr. Freq. Control.* **2010**, *57*, 2685–2694. [CrossRef]
17. Leong, T.; Wooster, T.; Kentish, S.; Ashokkumar, M. Minimising oil droplet size using ultrasonic emulsification. *Ultrason. Sonochemistry* **2009**, *16*, 721–727. [CrossRef]
18. Lad, V.N.; Murthy, Z.V.P. Enhancing the stability of oil-in-water emulsions emulsified by coconut milk protein with the application of acoustic cavitation. *Ind. Eng. Chem. Res.* **2012**, *51*, 4222–4229. [CrossRef]
19. Canselier, J.; Delmas, H.; Wilhelm, A.; Abismail, B. Ultrasound emulsification-an overview. *J. Dispers. Sci. Technol.* **2002**, *23*, 333–349. [CrossRef]
20. Ganz, S.; Gutierrez, E. *Cavitation: Causes, Effects, Mitigation and Application*; Rensselaer Polytech. Inst.: Hartford, CT, USA, 2012.
21. Abedini, M.; Reuter, F.; Hanke, S. Corrosion and material alterations of a CuZn38Pb3 brass under acoustic cavitation. *Ultrason. Sonochemistry* **2019**, *58*, 104628. [CrossRef]
22. Blake, F., Jr. The Properties of Gaseous Solutions as Revealed by Acoustic Cavitation Measurements. *J. Acoust. Soc. Am.* **1949**, *21*, 464. [CrossRef]
23. Noltingk, B.E.; Neppiras, E.A. Cavitation produced by ultrasonics. *Proc. Phys. Soc. Sect. B* **1950**, *63*, 674. [CrossRef]
24. Neppiras, E.; Noltingk, B. Cavitation produced by ultrasonics: Theoretical conditions for the onset of cavitation. *Proc. Phys. Soc. Sect. B* **1951**, *64*, 1032. [CrossRef]
25. Leith, W.C. Cavitation Damage of Metals. Ph.D. Thesis, McGill University, Montréal, QC, Canada, 1960.
26. Tian, Y.; Ketterling, J.A.; Apfel, R.E. Direct observation of microbubble oscillations. *J. Acoust. Soc. Am.* **1996**, *100*, 3976–3978. [CrossRef]
27. Mettin, R. Bubble structures in acoustic cavitation. In *Bubble and Particle Dynamics in Acoustic Fields: Modern Trends and Applications*; Research Signpost: Kerala, İndia, 2005.
28. Reuter, F.; Lesnik, S.; Ayaz-Bustami, K.; Brenner, G.; Mettin, R. Bubble size measurements in different acoustic cavitation structures: Filaments, clusters, and the acoustically cavitated jet. *Ultrasonics Sonochemistry* **2019**, *55*, 383–394. [CrossRef]
29. Tuziuti, T.; Yasui, K.; Iida, Y.; Sivakumar, M.; Koda, S. Laser-light scattering from a multibubble system for sonochemistry. *J. Phys. Chem. A* **2004**, *108*, 9011–9013. [CrossRef]
30. Harba, N.; Hayashi, S. Dust particles counteract the boosting of single-bubble sonoluminescence by glycerol droplets. *Jpn. J. Appl. Phys.* **2003**, *42*, 2971. [CrossRef]
31. Brotchie, A.; Grieser, F.; Ashokkumar, M. Effect of power and frequency on bubble-size distributions in acoustic cavitation. *Phys. Rev. Lett.* **2009**, *102*, 084302. [CrossRef]
32. Frohly, J.; Labouret, S.; Bruneel, C.; Looten-Baquet, I.; Torguet, R. Ultrasonic cavitation monitoring by acoustic noise power measurement. *J. Acoust. Soc. Am.* **2000**, *108*, 2012–2020. [CrossRef]
33. Vichare, N.P.; Senthilkumar, P.; Moholkar, V.S.; Gogate, P.R.; Pandit, A.B. Energy analysis in acoustic cavitation. *Ind. Eng. Chem. Res.* **2000**, *39*, 1480–1486. [CrossRef]
34. Laborde, J.L.; Bouyer, C.; Caltagirone, J.-P.; Gérard, A. Acoustic bubble cavitation at low frequencies. *Ultrasonics* **1998**, *36*, 589–594. [CrossRef]
35. Apfel, R. Acoustic cavitation: A possible consequence of biomedical uses of ultrasound. *Br. J. Cancer. Suppl.* **1982**, *5*, 140.
36. Son, Y.; Lim, M.; Khim, J. Investigation of acoustic cavitation energy in a large-scale sonoreactor. *Ultrason. Sonochemistry* **2009**, *16*, 552–556. [CrossRef]
37. Sunartio, D.; Ashokkumar, M.; Grieser, F. Study of the coalescence of acoustic bubbles as a function of frequency, power, and water-soluble additives. *J. Am. Chem. Soc.* **2007**, *129*, 6031–6036. [CrossRef]
38. Ashokkumar, M. The characterization of acoustic cavitation bubbles-an overview. *Ultrason. Sonochemistry* **2011**, *18*, 864–872. [CrossRef]
39. Zhou, D. A novel concept for boiling heat transfer enhancement. *J. Mech. Eng.* **2005**, *51*, 366–373.
40. Cui, J.; Zhang, Z.; Liu, X.; Liu, L.; Peng, J. Studies on viscosity reduction and structural change of crude oil treated with acoustic cavitation. *Fuel* **2020**, *263*, 116638. [CrossRef]
41. Yakut, M.; Tangel, A.; Tangel, C. A microcontroller based generator design for ultrasonic cleaning machines. *Istanb. Univ. J. Electr. Electron. Eng.* **2009**, *9*, 853–860.

42. Mason, T.J. Ultrasonic cleaning: An historical perspective. *Ultrason. Sonochemistry* **2016**, *29*, 519–523. [CrossRef]
43. Peng, Q.; Wang, H.; Su, X.; Lu, M. A new design of the high-power ultrasonic generator. In Proceedings of the 2008 Chinese Control and Decision Conference, Yantai, China, 2–4 July 2008; pp. 3800–3803.
44. Lin, S. Study on the multifrequency Langevin ultrasonic transducer. *Ultrasonics* **1995**, *33*, 445–448. [CrossRef]
45. Fabijański, P.; Łagoda, R. Intelligent Control Unit for Ultrasonic Cleaning System. *Przegląd Elektrotechniczny* **2012**, *88*, 115–119.
46. Shuyu, L. Load characteristics of high power sandwich piezoelectric ultrasonic transducers. *Ultrasonics* **2005**, *43*, 365–373. [CrossRef]
47. Fabijanski, P.; Lagoda, R. Modeling and Identification of Parameters the Piezoelectric Transducers in Ultrasonic Systems. In *Advances in Ceramics-Electric and Magnetic Ceramics, Bioceramics, Ceramics and Environment*; IntechOpen: London, UK, 2011; pp. 154–176.
48. Leighton, T. *The Acoustic Bubble*; Academic Press: Cambridge, MA, USA, 2012.
49. COMSOL Multiphysics. Introduction to COMSOL multiphysics®. *COMSOL Multiphysics* **1998**, *9*, 2018.



© 2020 by the authors. Licensee MDPI, Basel, Switzerland. This article is an open access article distributed under the terms and conditions of the Creative Commons Attribution (CC BY) license (http://creativecommons.org/licenses/by/4.0/).